NASA Technical Memorandum 84667

HEAT-TRANSFER DISTRIBUTIONS ON BICONICS AT INCIDENCE IN HYPERSONIC-HYPERVELOCITY He, N_2, AIR, AND CO_2 FLOWS

Charles G. Miller

John R. Micol

Peter A. Gnoffo

Sue E. Wilder

JUN 1983
RECEIVED
NASA STI FACILITY
ACCESS DEPT.

May 1983

NASA
National Aeronautics and
Space Administration

Langley Research Center
Hampton, Virginia 23665

HEAT-TRANSFER DISTRIBUTIONS ON BICONICS AT INCIDENCE

IN HYPERSONIC-HYPERVELOCITY He, N_2, AIR, AND CO_2 FLOWS

Charles G. Miller,* John R. Micol,**
Peter A. Gnoffo†, and Sue E. Wilder††
NASA Langley Research Center
Hampton, Virginia 23665

Abstract

Laminar heat-transfer rates were measured on spherically blunted, 13°/7° on-axis and bent biconics (fore cone bent 7° upward relative to aft cone) at hypersonic-hypervelocity flow conditions in the Langley Expansion Tube. Freestream velocities from 4.5 to 6.9 km/sec and Mach numbers from 6 to 9 were generated using helium, nitrogen, air, and carbon dioxide test gases, resulting in normal shock density ratios from 4 to 19. Angle of attack, referenced to the axis of the aft cone, was varied from zero to 20° in 4° increments. The effect of nose bend, angle of attack, and real-gas phenomena on heating distributions are presented along with comparisons of measurement to prediction from a code which solves the three-dimensional "parabolized Navier-Stokes" equations.

Nomenclature

C*	defined as $\mu^* T_\infty / \mu_\infty T^*$
C_h	heat-transfer coefficient, $\dot{q}/(h_{t,2} - h_w)$, J-sec/m⁴
h	enthalpy, J/kg
L	model length, m
M	Mach number
p	pressure, N/m²
$\dot{q}$	heat-transfer rate, W/m²
r	radius, m
R	unit Reynolds number, m⁻¹
St	Stanton number, $C_h/\rho_\infty U_\infty$
t	time, sec
T	temperature, K
T*	reference temperature, $(T_{t,2}/6)(1+3T_w/T_{t,2})$, K, Ref. 41
U	velocity, m/sec
$\bar{v}^*$	viscous interaction parameter, $C^* M_\infty / \sqrt{R_{\infty,L}}$
x,y,z	model coordinates (see Fig. 1), m
Z	moles of dissociated gas per moles of undissociated gas
α	angle of attack, deg
γ_E	isentropic exponent
μ	viscosity, N-sec/m²
μ^*	viscosity evaluated at T*, N-sec/m²
φ	circumferential angle measured from the most leeward meridian, deg
ρ	density, kg/m³
θ	cone half-angle, deg

Subscripts

a	aft-cone section
b	base
f	fore-cone section
m	measured
n	nose
s,10	incident shock into quiescent acceleration gas
sph	sphere
w	wall
2	static conditions immediately behind normal shock
t,2	stagnation conditions behind normal shock
∞	free-stream conditions

*Aero-Space Technologist, Aerothermodynamics Branch, Space Systems Division.
**Aerospace Engineer, Aerothermodynamics Branch, Space Systems Division.
†Aerospace Engineer, Aerothermodynamics Branch, Space Systems Division.
††Aero-Space Technologist, Aerothermodynamics Branch, Space Systems Division.

Introduction

Recent advances in navigation and knowledge of planetary atmospheres,[1-3] along with the need for Earth orbital transfer vehicles (OTV),[4-6] have rekindled interest in aerobraking and aerocapture techniques for proposed Earth and planetary missions. A generic vehicle proposed for missions to a number of planets[2,3] and a viable moderate lift-to-drag OTV candidate,[4-6] which also offers many advantages as a reentry

vehicle,[7] is a spherically-blunted biconic with
the fore-cone section bent upward relative to the
aft-cone section. Because of the scarcity of
experimental data for bent biconics, a study was
initiated at the Langley Research Center to
establish a comprehensive data base. To date,
aerodynamic coefficients, pressure distributions,
oil-flow patterns, and shock shapes have been
measured and reported on 2.9-percent scale models
of the proposed configuration and this configura-
tion without a bent nose (on-axis biconic).[8-10]
These measurements have been made in three con-
ventional-type, hypersonic wind tunnels, namely
the 20-Inch Mach 6 Tunnel, Continuous Flow Hyper-
sonic Tunnel, and Hypersonic CF₄ Tunnel, thereby
providing a range of Mach number, Reynolds
number, and normal shock density ratio (real-gas
simulation parameter). Although a number of
flowfield computer codes have been verified with
this data base, heat-transfer measurements are
required to determine if these codes accurately
predict viscous effects.

The purpose of the present study is twofold:
(1) to determine the effect of nose bend, angle
of attack, and real-gas flow phenomena on heating
distributions for the biconics; and (2) compare
measurement with prediction. Because heat-
transfer measurements for bent biconics are
particularly scarce in the open literature, the
present data represent a significant step toward
achieving the goal of a complete and accurate
data base for the validation of flowfield
computer codes.

<center>Experimental Method</center>

Facility

The Langley Expansion Tube[11,12] is
basically a 15.24-cm-diameter tube divided into
three sections by two diaphragms; thus, this
facility may be viewed as two shock tubes in
tandem. Thick steel diaphragms separate the
driver and intermediate sections, whereas a thin
Mylar diaphragm separates the intermediate and
acceleration sections. The isentropic, unsteady
expansion resulting from the rupture of this thin
Mylar diaphragm generates hypersonic and hyper-
velocity flow at the acceleration section exit
from the low Mach number, shock-tube flow which
encounters the secondary diaphragm. A detailed
description of this facility is presented in
Ref. 11, and calibration results are presented in
Refs. 12 to 14.

Models

A planform view and dimensions of the
biconic models are shown in Fig. 1, and a photo-
graph of the bent biconic model installed in the
test section of the expansion tube is shown in
Fig. 2. The bent-biconic model represents a
1.9-percent scale of the proposed Mars sample
return, single-mission vehicle.[2] The models were
fabricated from stainless steel except for the
nose tips, which were fabricated from MACOR, a
machinable glass-ceramic.[15] Each model contained
five slots for MACOR[15] substrates, the surfaces
of which were contoured to the respective conic
section. Two slots were machined along the most
windward ray, two along the most leeward ray,
(one on the fore cone and one on the aft cone),
and one along the 90° ray on the aft cone.

Instrumentation

Heat Transfer. Thin-film resistance
gages[16,17] were used to measure heat-transfer
rates during the 250-microsecond test period of
the expansion tube. Eight palladium gages, each
approximately 1200 Å thick, were deposited along
the polished surface of each MACOR substrate; a
single thin-film gage was deposited at the spher-
ical nose tip. Each gage was in the form of a
serpentine pattern, as shown in Ref. 16, and pro-
vided nearly a point measurement since the
sensing surface was 1.02 mm by 1.27 mm. Gages
were covered with Al₂O₃ approximately 5000 Å
thick to prevent the gage from becoming electri-
cally shorted due to the ionized flow over the
model. A constant current of 2 mA was maintained
through each gage, which is sufficiently low to
avoid ohmic heating effects.[16]

Heat-transfer rates on the nose, windward
ray of the fore cone, and every other gage on the
windward ray of the aft cone were determined by
numerically integrating the surface temperature
change as a function of time.[16,18] This method
accounts for the variation of substrate thermal
properties with temperature or time. Heat-
transfer rates for the remaining gages were
obtained using the analog circuit described in
Ref. 17; the surface temperature for these gages
was sufficiently low so to not require a signifi-
cant correction to the heating rate because of
changes in the thermal properties of the MACOR
substrates.[16] Signals from the thin-film gage on
the spherical nose and the 32 gages located along
the most windward and leeward rays were recorded
at 400 kHz (2.5 microseconds between data
samples) with a transient waveform recording
system. Digital data from this analog-to-digital
system were retrieved by a HP 9845 computer and
reduced to time histories of the heating rate
(Fig. 3). Output signals for the eight thin-film
gages located along the 90° ray were recorded
from an oscilloscope with the aid of a camera.

Flow Visualization. Shock standoff distance
was obtained using a single-pass schlieren system
with a Xenon arc lamp as a light source. This
point light source, having a duration of approxi-
mately 150 nanoseconds, was discharged just prior
to termination of the useful test period.[12] (See
Fig. 3.) Representative schlieren photographs
are shown in Fig. 4.

Facility Flow Quantities. Incident shock
velocity at the tube exit (test section) was
determined by applying a least-squares curve fit
to the average shock velocity between successive
instrumented stations.[19] The time for the shock
to travel between stations was obtained from
counter-timer readings of the "stop" signals
supplied by pressure transducers and heat-
transfer gages mounted flush with the tube wall.
Tube wall pressures and pitot pressures were
measured using piezoelectric (quartz) transducers
in conjunction with charge amplifiers. (It
should be noted at this point that pitot
pressures were measured during calibration tests
performed prior to this study but were not
measured for tests with the biconic models, as
discussed subsequently.) Freestream static
pressure was inferred from a transducer located
1.7-m upstream of the tube exit; the variation in

<center>2</center>

static pressure between this station and the tube exit is expected to be small (within experimental uncertainty).

Test Conditions

Facility. For the present tests, the driver gas was unheated hydrogen at a nominal pressure of 4.14 MN/m^2. The double diaphragm mode of operation was employed to reduce randomness in the pressure ratio across the primary diaphragm at time of rupture. Test gases were helium, nitrogen, dry air, and carbon dioxide. For a given test, the acceleration gas was the same as the test gas, but at a lower initial pressure.[12] Flow conditions for this study correspond to the optimum flow,[12] and no attempt was made to operate the facility at off-optimum conditions for any of the test gases in order to match Mach number and/or Reynolds number.

Flow conditions were determined using the thermochemical equilibrium program of Ref. 20, which has been modified to include helium. Inputs were freestream static pressure, freestream velocity, and pitot pressure. (Freestream static pressure was assumed equal to the measured tube wall pressure near the tube exit, freestream velocity was assumed equal to the incident shock velocity at the tube exit,[14,21] and pitot pressure corresponds to a mean value across the inviscid test core as inferred from tests with a pitot pressure survey rake performed prior to the present study.) Nominal values of measured inputs to the program of Ref. 20 and the corresponding freestream and post-normal shock flow conditions are given in Table 1. Based on the findings of Ref. 21, the freestream flow for helium, air, and CO_2 is assumed to be in thermochemical equilibrium; this assumption is also made for nitrogen test gas. Because of the relatively small values of freestream Reynolds number and small model size, laminar flow over the models is expected for all test gases.

Models. The models were tested at angles of attack from zero to 20°, where angle of attack is referenced to the axis of the aft-cone section. Both biconic models were tested for $0° \le \alpha \le 20°$ in 4° increments in air; for the other three test gases, the biconics were tested at $\alpha = 0°$, 4°, 12°, and 20°. The on-axis biconic was rolled at $\alpha = 12°$ in air to provide a more detailed circumferential heating distribution. At $\alpha = 0°$ the spherical nose tip of the on-axis biconic was located 1.27 cm downstream of the tube exit. Based on unpublished calibration results, these relatively long models were located within the inviscid test core for all angles of attack and located in a region free of axial variation of flow properties.

Data Reduction and Uncertainty

Heat Transfer. The numerical method used to compute heat-transfer rates from the output of the thin-film resistance gages is discussed in Ref. 16, and the analog method is discussed in Ref. 17. Also included in Ref. 16 is a discussion of the calibration procedure used to determine the temperature coefficient of resistance of each gage and contributors to the uncertainty in the heat-transfer rate inferred from thin-film

gages. Primary contributors for the present study are believed to be the uncertainty in the thermal properties of MACOR,[16] changes that occurred in gage properties for gages that were used in successive tests without recalibration, and the poor signal-to-noise ratio experienced during a number of tests.

Considering the probable sources of errors discussed in Ref. 16, the maximum uncertainty in measured heat-transfer rate for any given gage and test is believed to be less than 15 percent. The rms uncertainty in measured heat-transfer rate for both biconic models and all four test gases is 8 percent. Although an 8-percent uncertainty in heating along the most windward ray is believed realistic, a larger uncertainty is expected on the leeward ray, particularly at high angles of attack. This is due to the lower values of heating on the leeward ray and the nature of the flow in this complex, viscous-dominated flow region at high α.

Shock Shape. The shock detachment distance from the model surface was read manually from the schlieren photographs using a digitizing system having a sensitivity of 100 counts per 2.54 mm. The maximum uncertainty in measured shock detachment distance is believed to be less than 5 percent.

Flow Conditions. Uncertainties in the measured and calculated nominal freestream and post-shock flow conditions for the four test gases depend primarily on: (1) the precision associated with the measurement of the tube wall static pressure p_w, incident shock velocity $U_{s,10}$, and pitot pressure $p_{t,2}$, (2) run-to-run repeatability of these quantities, always a primary concern with impulse-type facilities, and (3) the validity of the assumptions made concerning the use of these measurements.

Careful and frequent calibrations of the pressure transducers demonstrated that measured values of p_w and $p_{t,2}$ are accurate to within 10 percent and 6 percent, respectively. Shock velocity $U_{s,10}$ is believed accurate to within 2.5 percent.[21] Nominal values of measured p_w and $U_{s,10}$ for each test gas were obtained from calibration tests with a pitot pressure survey rake, performed prior to this study, and from tests with the biconic models. Because the inviscid test core diameter is only 7.6 to 8.9 cm,[12,14] the relatively large models prohibited installation of a pitot pressure probe in the inviscid test core without disturbing the model flowfield. Thus, the nominal value of pitot pressure presented in Table 1 for each test gas was inferred from previous unpublished calibrations with a hydrogen driver. This procedure for determining flow conditions is the same as used in Ref. 21 for a helium driver.

Data scatter between the various calibration runs and runs with the biconic models was small (less than 8 percent for p_w and $p_{t,2}$ and 3.5 percent for $U_{s,10}$) due primarily to the double-diaphragm mode of operation.[12] Now, based on unpublished pressure distributions measured on a sharp leading-edge flat plate for the four test gases, the assumption that $p_\infty = p_w$ is believed valid. However, the assumptions that

3

U_∞ = $U_{s,10}$ and U_∞ are constant with run
time are subject to question.[22] The sensitivity
of calculated freestream and post-shock flow
conditions, including stagnation-point heat-
transfer rate to a sphere, to these uncertainties
in measured inputs are presented in Ref. 21.

Calculated Stagnation-Point Heat Transfer to a Sphere.

Heating distributions on the biconics
are presented in terms of the freestream Stanton
number St_∞ and as the ratio of surface heat-
transfer rate to predicted stagnation-point heat-
transfer rate to a sphere with radius equal to
the biconic nose radius, $\dot{q}/\dot{q}_{sph}$. The wall
enthalpy h_w required to compute St_∞ corre-
sponds to a wall temperature equal to 300 K.
Values of $\dot{q}_{sph}$ for the four test gases were
obtained from the thermochemical equilibrium
calculations of Ref. 23 and are presented in
Table 1.

Prediction Method

Heating distributions were computed using
computer code that solves the steady,
three-dimensional "parabolized Navier-Stokes
equations."[24,25] This code requires supersonic
flow above the boundary layer in the downstream
marching direction from the starting plane of
data at or in front of the sphere-cone junction.
A total of 50 points were taken between the shock
and surface along an axis-normal coordinate and
the number of points in the boundary layer was
varied with angle of attack to account for the
thinning of the boundary layer. The
circumferential increment was 4.74°.

At the time the data reduction phase of the
present study was initiated, the PNS code was
applicable only for perfect air. This code has
since been modified to include helium and
real air in thermochemical equilibrium. Only a
few cases for real air have been run at the time
of this writing, and these results must be viewed
as preliminary.

Results and Discussion

The limited space of this report prohibits
presenting all the data obtained for the two
biconic models in the four test gases; thus, the
effects of nose bend, angle of attack, and test
gas are illustrated with sample longitudinal
heating distributions and with summary plots.
Because these data provide the opportunity to
validate various perfect-gas and real-gas
flowfield computer codes and recognizing the
difficulty associated with the extraction of data
from such a report, tabulations of the present
data are available upon request. Before
presenting the data, a few general comments will
be made.

A primary purpose of this study was to
examine real-gas effects, resulting from the
excitation of vibration, dissociation, and
ionization energy modes, on heating to biconics
in gases corresponding to various planetary
atmospheres. CO_2 was selected as a test gas
since it is the primary constituent of Mars and
Venus atmospheres, nitrogen is the primary
constituent of Titan's atmosphere, and air is, of
course, Earth's atmosphere. To provide a lower

limit to the range of normal-shock density ratio
and a means for comparison with perfect-gas
flowfield predictions, helium was used as a test
gas. Even at the present velocity of 6.9 km/s,
helium was not ionized. Thus, the biconic models
were tested in ideal-gas and real-gas flow
environments in the same facility with the same
instrumentation, data acquisition system, and
data reduction procedures.

In general, the flow was observed to
establish (C_h become essentially constant with
time) on the windward side of both biconic models
within 120 µs for all test gases and 0° < α <
20°. Flow establishment on the leeward side
required more time, especially at the higher
angles of attack where the flow is quite complex
and viscous dominated,[26-28] and the output of the
leeward gages was characterized by larger
fluctuations with time. However, even at the
highest value of α, there was evidence that the
"coarse" inviscid flow and finer viscous-flow
structure about the model generally established,
achieving a steady state within 200 µs. Thus,
the heating distributions presented herein are
assumed to represent a fully established flow
condition.

To avoid or minimize the effects of surface
temperature discontinuities on measured heat-
transfer rates,[29] the thermal conductivities of
the substrates and models should be matched as
close as possible. Another concern at the high
enthalpies of this study is the difference in
surface catalycity between the MACOR substrates
and the stainless-steel models.[30,31] Because
of these concerns, the model was covered with a
relatively thick deposit of Paralene C or sprayed
with Krylon, a crystal-clear acrylic, prior to
installation of the substrates. (It should be
noted that windward substrates were generally
destroyed during the post-run period and the
cover badly sandblasted; thus, the models were
removed from the facility after each run,
recovered, and new substrates installed.) The
effect of removing the cover is shown in Fig. 5
for the bent biconic in air. Removing the cover
produced no significant effect on heating. One
possible explanation for this good agreement is
the thin-film gages were placed a sufficient
distance from the material mismatches in the
model surface to allow the flow to adjust, if
necessary, to the MACOR surfaces. For the sake
of continuity and the fact the cover provided
excellent protection of the model surface from
solid contaminants carried in the post-test flow,
the model was covered for all runs.

Because of the relatively small model size
and close proximity of the shock to the model
surface at the higher density ratios, the flow
within the shock layer may depart from
equilibrium. This is especially true in the nose
region. The results of Ref. 21, based on binary
scaling for blunt bodies, revealed that the
product of freestream density and predicted
equilibrium shock standoff distance at the
stagnation point must exceed 10^{-5} kg/m² to avoid
significant nonequilibrium flow effects. For the
biconic spherical nose radius of 3.83 mm, this
product is less than 1.3×10^{-6} kg/m² for the
three dissociated test gases, thus well within
the nonequilibrium flow regime.

4

At sufficiently low Reynolds numbers, the shock and boundary-layer thicknesses are no longer negligible compared with the shock detachment distance.[21] A number of researchers have suggested various criteria in an effort to define the regimes between continuum and free molecular flow,[32] but these are only approximations. The parameter $\sqrt{R_{2,rn}}/(\rho_2/\rho_\infty)^2$ (see Ref. 33) was selected to estimate the viscous effects for the flow over the spherical nose. According to this parameter, which varies from a low of 2.6 for CO_2 to a high of 23 for helium, the present flow over the nose is just within the slip flow regime.[3,33] In this regime, relatively small changes in Reynolds number may result in large changes in surface heating. The increase in heating over the continuum value is small (< 5 percent, or so) for helium, but may be significant for the other test gases, particularly CO_2. Although this parameter accounts for real-gas effects via use of ρ_2/ρ_∞,[21] it does not include the effect of wall temperature ratio $T_w/T_{t,2}$. The present large wall cooling tends to decrease the boundary-layer thickness, hence diminish rarefaction effects.[21]

Effect of Nose Bend

Bending the fore-cone section upward provides aerodynamic advantages[2,3] because of the asymmetry, but at an expected penalty in higher heating rates to the fore-cone section. To examine effects of this nose bend, heating distributions for the bent biconic are compared to the on-axis biconic in Figs. 6 and 7 for various angles of attack. Longitudinal heating distributions along the most windward and leeward rays are shown for air in Fig. 6. The ratio of windward heat-transfer coefficient for the bent biconic to that for the on-axis biconic is shown in Fig. 7 for all four test gases. These results (Fig. 7) were obtained from curve fits to the data to smooth the results and account for any missing thin-film gages for a particular run.

Noticeably lacking from the fore-cone heating distributions at $\alpha = 0°$ for all test gases was the overexpansion-recompression trend observed in the pressure distributions for these biconics at Mach 6 and Mach 10[8-10] and attributed to the surface discontinuity at the sphere-cone junction. For laminar flow, heating is expected to follow the trend in pressure;[34,35] however, the Mach 10 results of Refs. 36 and 37 imply that the present heating distributions should be free of such trends for x/L > 0.25. The decrease in windward heating due to the expansion at the junction scales roughly with the surface inclination change. That is, between the last gage on the fore cone and first gage on the aft cone, St_∞ decreases roughly 1.3 to 1.5 for the on-axis biconic (surface inclination change of 5.8°) and approximately twice this for the bent biconic (change of 12.8°, or twice that of the on-axis biconic) for all four test gases.

On the leeward side, bending the nose upward at $\alpha = 0°$ causes a larger variation in heating with z/L on the most leeward ray of the fore cone, smaller variation on the aft cone, and a decrease in heating by a factor of 2 to 3 for all test gases. When α is increased to 4°, corresponding to the leeward side of the bent biconic

being nearly shielded from the flow, the heating distributions for the two biconics begin to converge with increasing distance from the nose tip. At $\alpha = 12°$ (Fig. 6(b)), corresponding to the on-axis biconic leeward side being almost shielded from the flow and the bent biconic being fully shielded, heating still decreases with increasing x/L for the on-axis biconic but increases with z/L for the bent biconic. These trends cause the heating distributions for the two biconics to cross at about 40 percent of the body length. At $\alpha = 20°$ (Fig. 6(a)), leeward heating for the bent biconic exceeds that for the on-axis biconic in air. Similar trends were observed for the other gases and are consistent with leeward flow separation,[8-10,26-28,37] as will be discussed in the next section.

The penalty paid in increased windward fore-cone heating due to the nose bend is about 1.7 to 2 at $\alpha = 0°$ for the four test gases (Fig. 7(a)). However, the nose bend causes a decrease in windward aft-cone heating for air, N_2, and CO_2, whereas the heating for helium is essentially unaffected by the bend. This lower heating on the bent biconic aft cone for the dissociated test gases is believed due to: (1) the lower values of gamma within the shock layer for these gases, which result in a larger expansion at the junction, hence a lower aft-cone surface pressure,[10] and (2) nonequilibrium flow effects. At $\alpha = 12°$, the penalty in fore-cone heating due to the bend decreases to about 1.2 to 1.4 and to about 1.1 to 1.2 at $\alpha = 20°$. Heating on the aft cone is less for the bent biconic, including helium test gas, for $\alpha = 12°$ and 20°. Thus, although a penalty in windward heating to the fore cone occurs due to the nose bend, as expected, this penalty diminishes markedly with increasing α and is only 10 to 20 percent at the design trim angle of attack of 20° for the bent biconic.

Effect of Angle of Attack

Heating to the windward ray increases with angle of attack for both biconics and all test gases, as expected, but the relative effect of α on heating decreases with increasing α (Figs. 8 to 10). For the present range of α, the penalty in windward heating for the bent biconic is roughly a factor of 2 on the fore cone and a factor of 3 to 4 on the aft cone, being largest for helium test gas.

The effect of α on leeward heating is not nearly as orderly as on the windward side. Leeward heating for the on-axis biconic decreases as α is increased from 0° to 8°, but increases for $\alpha > 8°$. This trend was observed for all test gases and is attributed to flow separation and the formation of vortices.[8-10,26-28,37] The oil-flow patterns of Refs. 9 and 10 show that a "stagnation-line" type of flow is created on the most leeward ray by the mutual action of counter-rotating longitudinal vortices that reattach on this ray. For the low Reynolds numbers of this study, the leeward separated flow should be free of any secondary vortices.[10] This vortex reattachment results in the heating on the most leeward ray being higher than just off this ray, as evident from the circumferential heating distribution shown in Fig. 11 for the on-axis biconic at $\alpha = 12°$.

Effect of Test Gas

Shock shapes for the four test gases are compared in Fig. 12 for the bent biconic at $\alpha = 4°$. The fact that the shock detachment distance for blunt bodies in hypersonic flows correlates in terms of a single parameter ρ_2/ρ_∞ is well known,[2,3,21] with the detachment distance decreasing with increasing density ratio. This decrease in shock detachment distance with increasing ρ_2/ρ_∞ also occurs for the relatively slender biconic models as shown in Fig. 12. The effect of density ratio on detachment distance was observed to diminish with increasing angle of attack on the windward and leeward sides; that is a lesser effect of ρ_2/ρ_∞ on windward shock-detachment distance occurs as the effective body becomes blunter. The trend on the leeward side is due to the shock inclination downstream of the nose region becoming more dependent on Mach number at the higher α.[8] The observed differences in shock detachment distance and inclination for the present test gases are expected to influence the variable edge-entropy effect caused by the mass "swallowed" or entrained by the boundary layer,[38,39] hence influence the heating distributions.

In examining the effects of nose bend and angle of attack on heating distributions, differences in Mach number, Reynolds number, density ratio or gamma, and wall temperature ratio were not considered explicitly. However, these quantities must be considered in any attempt to deduce the effect of test gas on heating. This adds complexity to the present study since the Expansion Tube was operated to yield the highest quality flow for each test gas and M_∞ and R_∞ were not matched for the four gases. For example, although the freestream Reynolds numbers for helium, air and CO_2 are relatively close, R_∞ for nitrogen is only half as large. Now, laminar heating on a reentry glider model has been correlated in terms of $St_\infty \sqrt{R_{\infty,L}}$ for high enthalpy flows.[40] Taking this a step further to account for differences in R_∞, M_∞, and $T_w/T_{t,2}$, the decision was made to present the present heating data in terms of $St_\infty/\overline{V}^*$. The viscous interaction parameter $\overline{V}^*$ is defined[32] as $C^*M_\infty/\sqrt{R_{\infty,L}}$, where $C^* \equiv \mu^*T_\infty/\mu_\infty T^*$ and T^* is a reference temperature,[41] $T^* = (T_{t,2}/6)(1+3T_w/T_{t,2})$. Heating distributions are also presented as the percent of stagnation-point heat-transfer rate to a sphere[23] having a radius equal to that of the spherical nose tip, $\dot{q}/\dot{q}_{sph}$. (Values of $\dot{q}_{sph}$ are presented in Table 1.) (Although $\dot{q}_{sph}$ is relatively insensitive to Mach number and Reynolds number, the ratio $\dot{q}/\dot{q}_{sph}$ may not be, and thus does not provide a means for separating M_∞, R_∞ effects from real-gas effects.)

Values of the heating ratio $\dot{q}/\dot{q}_{sph}$ for the four test gases are compared in Fig. 13 for the on-axis biconic. At zero incidence (Fig. 13(a)), $\dot{q}/\dot{q}_{sph}$ on the fore cone is nearly the same for air, N_2, and CO_2, all being higher than helium. As the flow expands at the fore-cone/aft-cone junction, the decrease in heating that occurs for CO_2 is greater than for the other three gases and $\dot{q}/\dot{q}_{sph}$ for CO_2 approaches that for helium. As discussed previously, this trend is attributed to gamma effects and possible nonequilibrium flow

effects. The same trends in windward $\dot{q}/\dot{q}_{sph}$ are observed at $\alpha = 12°$ and 20°; however, the difference in $\dot{q}/\dot{q}_{sph}$ between the test gases decreases with increasing α, especially on the fore cone. At $\alpha = 12°$, leeward $\dot{q}/\dot{q}_{sph}$ exhibits the same trend as observed on the windward side, but at $\alpha = 20°$, this heating ratio for CO_2 is less than for the other gases. As a rule of thumb for the on-axis biconic, $\dot{q}/\dot{q}_{sph}$ on the windward aft cone is roughly half that on the windward fore cone and leeward values are an order of magnitude less than windward values.

Basically, the same trends in $\dot{q}/\dot{q}_{sph}$ were observed for the bent biconic as observed for the on-axis biconic. One notable exception was that $\dot{q}/\dot{q}_{sph}$ for CO_2 is lower than the other gases on the windward and leeward sides of the aft cone for all angles of attack. As with the on-axis biconic, $\dot{q}/\dot{q}_{sph}$ on the leeward side of the bent biconic for air and N_2 either agrees with or exceeds values for helium. One last point—windward aft-cone heating distributions in CO_2 at the higher angles of attack decrease monotonically downstream of the junction, but then increase in the direction of the base. Schlieren photographs in CO_2 (Fig. 4) revealed the shock over the aft cone on the windward side curved back toward the model surface in the region of the base. This minima in heating on the windward side of the aft cone is believed to be characteristic of low gamma flows since it was observed[10] in pressure distributions measured at Mach 6 in CF_4 ($\gamma_{eff} = 1.13$), but not at Mach 6 in air ($\gamma = 1.4$). It was also predicted for CF_4 using a perfect-gas, inviscid flowfield code with effective gamma as the input,[10] and predicted in Ref. 3 for CO_2.

In Figs. 14 and 15, windward $St_\infty/\overline{V}^*$ for air, nitrogen, and CO_2 is nondimensionalized by this ratio for helium. In this form, the results for CO_2 are consistently lower than for air or nitrogen for both biconics and $0° \leq \alpha \leq 20°$. The air and nitrogen results are generally in fair to good agreement for both biconics, particularly on the fore cone. This good agreement between air and nitrogen is expected, provided Reynolds number effects are properly accounted for, because of the similarity in gamma within the shock layer for these two gases, in Mach number, and in $T_w/T_{t,2}$. When these two gases are not in agreement on the aft cone, the air data usually exceed the nitrogen data, thereby implying a larger departure from equilibrium for nitrogen in the expansion at the junction. The ratio $St_\infty/\overline{V}^*$ for air, nitrogen and CO_2 is less than that for helium.

Due to the complexity of the present flow, it is difficult to separate Mach number, Reynolds number, gamma, and chemistry effects. Additional tests with these, or similar, models at various Mach numbers and Reynolds numbers in conventional, ideal-air wind tunnels are required to separate out the real-gas effects and determine if $\overline{V}^*$ accurately accounts for M_∞ and $R_{\infty,L}$ effects.

Comparison to Prediction

Comparisons of measured and predicted heating distributions in helium are shown in Figs. 16 and 17 for the on-axis biconic and bent

biconic, respectively. This code ran success-
fully for $0° < \alpha < 20°$ for the on axis biconic,
but difficulties were encountered at the highest
angle of attack for the bent biconic. The fail-
ure to run successfully at $\alpha = 20°$, corresponding
to $\alpha_f = 27°$, is attributed to the proximity of
the sonic line across the shock layer to the
starting data plane on the windward side.[10] The
stagnation-point heat-transfer rate measured
at the spherical nose tip of the on-axis biconic
in helium at $\alpha = 0°$ was predicted to within 3
percent by the starting solution[42] used for the
PNS code. Heating rates on the on-axis biconic
(Fig. 16) at $\alpha = 0°$ and $4°$ are accurately
predicted by the PNS code. At $\alpha = 12°$, corres-
ponding to a thinner boundary layer on the wind-
ward side (requires more points to accurately
model the temperature distribution through the
boundary layer) and separated, viscous-dominated
flow on the leeward side, the PNS code slightly
underpredicts windward and leeward heating. With
the exception of a few points, the agreement is
within 10 percent or within the experimental
uncertainty. At $\alpha = 20°$, the underprediction of
windward heating worsens and measurement and pre-
diction diverge on the leeward side of the aft
cone.

Turning to the bent biconic (Fig. 17), the
PNS code again accurately predicts the heating
distributions at $\alpha = 0°$ and $4°$ in helium. Wind-
ward aft-cone heating is accurately predicted for
$0° \le \alpha \le 12°$, whereas windward fore-cone heating
is underpredicted somewhat. At $\alpha = 12°$, the PNS
code overpredicts leeward heating by as much as
15 to 20 percent. Thus, in general, when the
leeward side is not fully shielded from the flow
($\alpha_f/\theta_f < 1$), the PNS code predicts windward
and leeward heating with good accuracy. When the
leeward side is shielded, resulting in vortex
shedding, the PNS code tends to overpredict
leeward heating.

Nonequilibrium flow effects were expected
for these models in air, but it was hoped that
comparisons to the PNS code with equilibrium
real-air capability would furnish information on
the degree to which nonequilibrium influenced the
heating. The reasoning, somewhat oversimplified,
was if the code was verified for helium flow and
care taken to incorporate the real-air proper-
ties, then the code should provide the basis for
deducing nonequilibrium flow effects. At the
time of this writing only two air cases had been
run for the on-axis biconic and both cases must
be viewed as preliminary. At $\alpha = 0°$ and $4°$
(Fig. 18), measured and predicted heating on the
fore cone tend to diverge with distance from the
nose tip. Since the PNS code tended to underpre-
dict heating in helium, this trend may be the
result of a nonequilibrium expansion from the
spherical nose onto the fore cone and the flow
tending to equilibrate as it approaches the junc-
tion. Windward aft-cone heating is underpredic-
ted by up to 25 percent for both angles of
attack. Leeward heating on the fore cone is
predicted quite well (within 10 percent) at $\alpha =
4°$, but the aft-cone heating is underpredicted 15
to 20 percent. The cause(s) for these underpre-
dictions in air are not fully understood at this
time and additional analysis is planned.

Concluding Remarks

Laminar heating distributions have been
measured on spherically-blunted, $13°/7°$ on-axis
and bent biconics in the Langley Expansion Tube.
These data are unique since a given model was
tested in several test gases at hypersonic and
hypervelocity flow conditions. Test gases were
helium, nitrogen, air, and carbon dioxide; free-
stream Mach numbers ranged from 6 to 9 and
velocities from 4.5 to 7 km/s. Even at these
high velocities, helium behaved as an ideal gas,
providing heating distributions that may be
compared to ideal-gas theory. Preliminary analy-
sis of these data revealed the following: (1)
Although a penalty in windward heating to the
fore cone due to the nose bend was observed, as
expected, this penalty diminishes rapidly with
increasing angle of attack and is only 10 to 20
percent at the design trim angle of attack of
$20°$. (2) Aft-cone windward heating was more
sensitive to angle of attack than fore-cone heat-
ing, increasing by 3 to 4 as the angle of attack
was increased from zero to $20°$ compared to 2 on
the fore cone. (3) Leeward heating distributions
initially decreased with increasing angle of
attack, but then increased. This trend is
attributed to flow separation on the leeward side
and the formation of vortices when the fore-cone
angle of attack exceeds the fore-cone half
angle. (4) Heating on the windward side of the
on-axis aft cone was roughly half that on the
fore cone and the leeward heating was an order of
magnitude less than the windward. (5) Several
trends were attributed to real-gas phenomena,
such as the decrease in aft-cone heating for CO_2
because of a nonequilibrium expansion at the
fore-cone/aft-cone junction. However, Mach
number, Reynolds number, wall temperature ratio,
and gamma or density ratio varied for the four
test gases. This makes it difficult to separate
real-gas effects from effects that result from
the variations and additional analysis is
required in this area. Finally, (6) the PNS code
predicts windward and leeward heating in helium
to good accuracy when the leeward side is not
shielded from the flow. When shielded, corres-
ponding to vortex shedding on the leeward side,
the PNS code tends to overpredict leeward heat-
ing. Preliminary results from the real-gas PNS
code yielded somewhat poorer comparisons to data
for air than those obtained by the perfect gas
code for helium.

References

[1]Walberg, G. D., "A Review of Aeroassisted
Orbit Transfer," AIAA Paper 82-1378, August 1982.

[2]Florence, D. E., "Aerothermodynamic Design
Feasibility of a Mars Aerocapture/Aeromaneuver
Vehicle," AIAA Paper 81-1127, June 1981.

[3]Florence, D. E., "Aerothermodynamic Design
Feasibility of a Generic Planetary Aerocapture/
Aeromaneuver Vehicle," AIAA Paper 81-1127, June
1981.

[4]Austin, R. E., Cruz, M. I., and French, J.
R., "System Design Concepts and Requirements for
Aeroassisted Orbital Transfer Vehicles," AIAA
Paper 82-1379, August 1982.

[5]Letts, W. R., and Peleksnos, A.,
"Aeroassisted Orbital Transfer Mission
Evaluation," AIAA Paper 82-1380, August 1982.

[6]Jamison, C. C., and Visentine, J. T.,
"Utilization of Shuttle Launched Research
Vehicles for the Technical Validation of Advanced
Earth and Planetary Atmospheric Entry Systems,"
AIAA Paper 82-1383, August 1932.

[7]Lin, T. C., and Grabowsky, W. R., "The
Search of Optimum Configurations for Reentry
Vehicles," AIAA Paper °2-1303, August 1982.

[8]Miller, C. G., and Gnoffo, P. A., "Pressure
Distributions and Shock Shapes for 12.84°/7°
On-Axis and Bent-Nose Biconics in Air at Mach 6,"
NASA TM 83222, December 1981.

[9]Miller, C. G., and Gnoffo, P. A., "An
Experimental Investigation of Hypersonic Flow
Over Biconics at Incidence and Comparison to
Prediction," AIAA Paper 82-1382, August 1982.

[10]Miller, C. G., Blackstock, T. A., Helms,
V. T., and Midden, R. E., "An Experimental
Investigation of Control Surface Effectiveness
and Real-Gas Simulation for Biconics," AIAA Paper
83-0213, January 1983.

[11]Moore, J. A., "Description and Initial
Operating Performance of the Langley 6-Inch
Expansion Tube Using Heated Helium Driver Gas,"
NASA TM X-3240, September 1975.

[12]Miller, C. G., "Operational Experience in
the Langley Expansion Tube With Various Test
Gases," NASA TM 78637, December 1977.

[13]Miller, C. G., "Flow Properties in
Expansion Tube with Helium, Argon, Air, and CO_2,"
AIAA Journal, Vol. 12, No. 4, April 1974, pp.
564-566.

[14]Shinn, J. L., and Miller, C. G.,
"Experimental Perfect-Gas Study of Expansion-Tube
Flow Characteristics," NASA TP 1317, December
1978.

[15]Crossman, D. G., "Machining a Machinable
Glass-Ceramic," Vacuum, Vol. 28, No. 2, February
1978, pp. 55-61.

[16]Miller, C. G., "Comparison of Thin-Film
Resistance Heat-Transfer Gages With Thin-Skin
Transient Calorimeter Gages in Conventional
Hypersonic Wind Tunnels," NASA TM 83197, December
1981.

[17]Reddy, N. M., "Heating-Rate Measurements
Over 30° and 40° (Half-Angle) Blunt Cones in Air
and Helium in the Langley Expansion Tube
Facility," NASA TM 80207, March 1980.

[18]Cook, W. J., "Determination of
Heat-Transfer Rates From Transient Surface
Temperature Measurements," AIAA Journal, Vol. 8,
No. 7, July 1970, pp. 1366-1368.

[19]Miller, C. G., and Jones, J. J., "Incident
Shock-Wave Characteristics in Air, Argon, Carbon
Dioxide, and Helium in a Shock Tube With Unheated
Helium Driver," NASA TN D-809, December 1975.

[20]Miller, C. G., "Computer Program of Data
Reduction Procedures for Facilities Using
CO_2-N_2-O_2-Ar Equilibrium Real-Gas Mixtures," NASA
TM X-2512, March 1972.

[21]Miller, C. G., "Shock Shapes on Blunt
Bodies in Hypersonic-Hypervelocity Helium, Air,
and CO_2 Flows, and Calibration Results in Langley
6-Inch Expansion Tube," NASA TN D-7800, February
1975.

[22]Friesen, W. J., "Use of Photoionization in
Measuring Velocity Profile of Free-Stream Flow in
Langley Pilot Model Expansion Tube," NASA TN
D-4936, December 1968.

[23]Sutton, K., and Graves, P. A., "A General
Stagnation-Point Convective-Heating Equation for
Arbitrary Gas Mixtures," NASA TR R-376, November
1972.

[24]Vigneron, Y. C., Rakich, J. V., and
Tannehill, J. C., "Calculation of Supersonic
Viscous Flow Over Delta Wings With Sharp Subsonic
Leading Edges," AIAA Paper 78-1137, July 1978.

[25]Agarwal, R., and Rakich, J. V., "Supersonic
Laminar Viscous Flow Past a Cone at Angle of
Attack in Spinning and Coning Motion," AIAA
Journal, Vol. 20, No. 6, June 1982, pp. 761-768.

[26]Stetson, K. R., "Boundary-Layer Separation
on Slender Cones at Angle of Attack," AIAA
Journal, Vol. 10, No. 5, May 1972, pp. 642-648.

[27]Rainbird, W. J., "Turbulent Boundary-Layer
Growth and Separation on a Yawed Cone," AIAA
Journal, Vol. 6, No. 12, December 1968, pp.
2410-2416.

[28]Rainbird, W. J., Crabbe, R. S., Peake, D.
J., and Meyer, R. F., "Some Examples of
Separation in Three-Dimensional Flow," Canadian
Aeronautics and Space Journal, December 1966,
pp. 409-423.

[29]Schultz, D. L., and Jones, T. V.,
"Heat-Transfer Measurements in Short-Duration
Hypersonic Facilities," AGARD-AG-165, February
1973.

[30]Anderson, L. A., "Effect of Surface
Catalytic Activity on Stagnation Heat-Transfer
Rates," AIAA Journal, Vol. 11, No. 5, May 1973,
pp. 649-656.

[31]Shinn, J. L., Moss, J. N., and Simmonds,
A. L., "Viscous-Shock-Layer Heating Analysis for
the Shuttle Windward Symmetry Plane with Surface
Finite Catalytic Recombination Rates," AIAA Paper
82-0842, June 1982.

[32]Little, H. R., "An Experimental
Investigation of Surface Conditions on
Hyperboloids and Paraboloids at a Mach Number of
10," AEDC-TR-69-225, January 1970.

[33]Gilbert, L. M., and Goldberg, L., "A
Reynolds Number Scaling Theory for Hypersonic
Ablation," AIAA Paper 67-155, January 1967.

[34]Widhopf, G. F., "Heat-Transfer Correlations
for Blunt Cones at Angle of Attack," Journal of
Spacecraft and Rockets, Vol. 8, No. 9, September
1971, pp. 1002-1004.

[35]Griffith, B. J., and Lewis, C. H., "Laminar Heat Transfer to Spherically Blunted Cones at Hypersonic Conditions," *AIAA Journal*, Vol. 2, No. 3, March 1964, pp. 438-444.

[36]Cleary, J. W., "Effects of Angle of Attack and Bluntness on Laminar Heating-Rate Distributions of a 15° Cone at a Mach Number of 10.6," NASA TN D-5450, October 1969.

[37]Dearing, D. J., "Laminar Heat-Transfer Distributions for a Blunted-Cone, Cone-Frustum Reentry Configuration at Mach 10," NASA TN D-5146, April 1969.

[38]Adams, J. C., Martindale, W. R., Mayne, A. W., and Marchand, E. O., "Real-Gas Scale Effects on Hypersonic Laminar Boundary-Layer Parameters Including Effects of Entropy-Layer Swallowing," AEDC-TR-75-2, December 1975.

[39]Griffith, B. J., and Majors, B. M., "Hypersonic Turbulent Boundary-Layer Parameters on Spherically Blunted Cones, Including Entropy Layer Swallowing and Real-Gas Effects," AIAA Paper 81-1089, June 1981.

[40]Stalker, R. J., "Development of a Hypervelocity Wind Tunnel," *Aeronautical Journal of the Royal Aeronautical Society*, June 1972, pp. 374-384.

[41]Cheng, H. K., "Hypersonic Flow With Combined Leading-Edge Bluntness and Boundary-Layer Displacement Effect," CAL Report No. AF-1285-A-4, August 1960.

[42]Gnoffo, P. A., "A Vectorized, Finite-Volume, Adaptive Grid Algorithm Applied to Planetary Entry Problems," AIAA Paper No. 82-1018, June 1982.

Table 1. Nominal Flow Conditions

Free-stream

Test Gas	P_∞, N/m^2	ρ_∞, kg/m^3	T_∞, K	$\gamma_{E,\infty}$	U_∞, m/sec	M_∞	R_∞, m^{-1}
Helium	1300	1.72×10^{-3}	364	1.667	6900	6.15	4.87×10^5
Nitrogen	1635	2.88	1913	1.302	5515	6.41	2.62
Air	2182	4.73	1604	1.296	5326	6.89	4.50
CO_2	1030	5.09	1070	1.179	4535	9.29	5.64

Post-Normal Shock

Test Gas	$P_{t,2}$, kN/m^2	$\rho_{t,2}$, kg/m^3	$T_{t,2}$, K	$\gamma_{E,t,2}$	$Z_{t,2}$	$h_{t,2}$, MJ/kg	h_w, MJ/kg	$\frac{\rho_2}{\rho_\infty}$	$\dot{q}_{sph}$, Ref. 23, MW/m^2
Helium	72.6	0.71×10^{-2}	4948	1.667	1.00	25.69	1.56	3.71	26.28
Nitrogen	85.6	3.55	6471	1.127	1.26	17.41	.31	11.83	28.22
Air	130.35	5.49	6162	1.143	1.34	15.96	.30	11.13	31.92
CO_2	103.0	9.83	3531	1.132	1.57	2.41	-8.72	18.83	21.92

Note: h_w evaluated at T_w = 300 K.
 Z_∞ = 1 for all test gases.
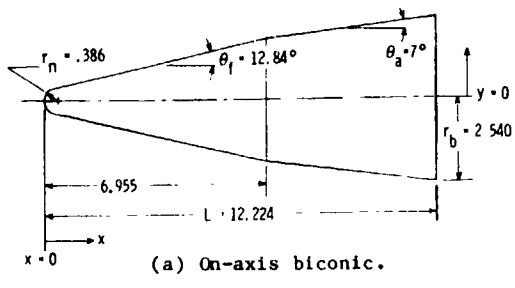
(a) On-axis biconic.

Fig. 1 Planform view and dimensions of models.
All dimensions in cm.
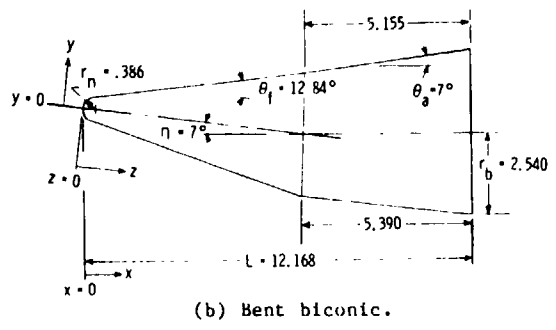
(b) Bent biconic.

Fig. 1 Concluded.
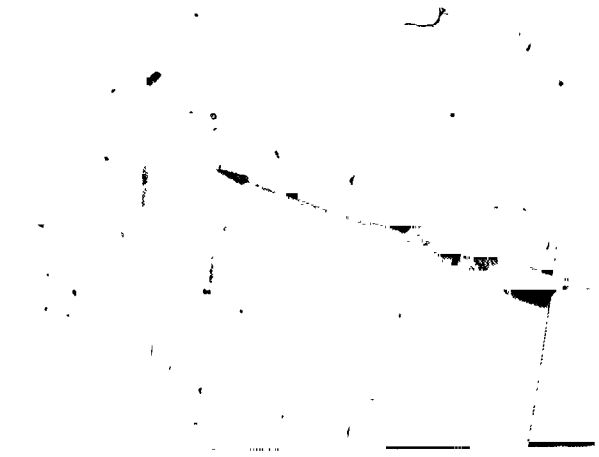
Fig. 2 Photograph of bent biconic model.
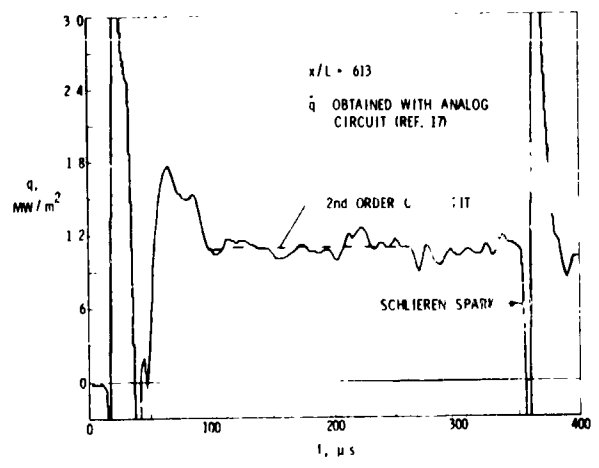
Fig. 3 Time history of heat-transfer rate on
leeward ray of on-axis biconic in air at
$\alpha = 4°$.

(a) $\alpha = 4°$.

Fig. 4 Representative schlieren photographs for
bent biconic in CO_2.
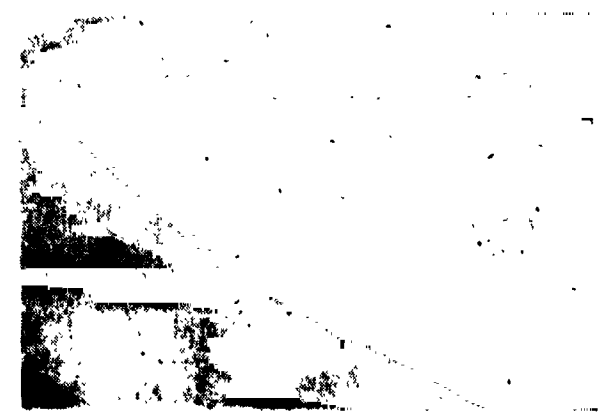
(b) $\alpha = 20°$.

Fig. 4 Concluded.

10
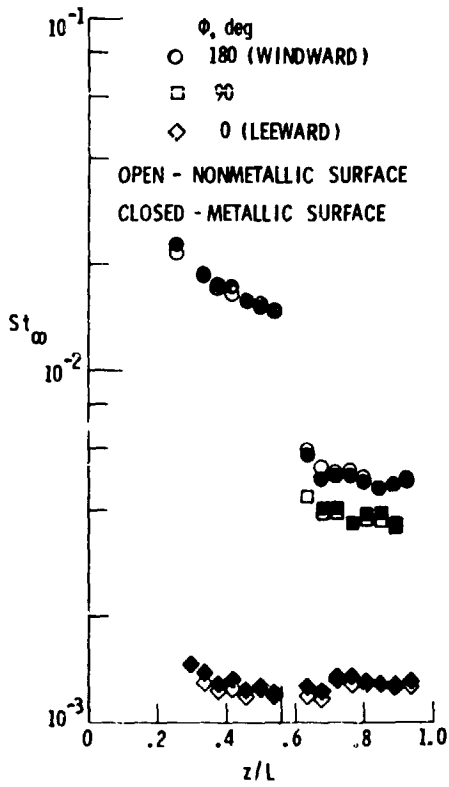
Fig. 5 Effect of model cover on heating for bent biconic in air at $\alpha = 8°$.

(b) $\alpha = 12°$.

Fig. 6 Continued.

(a) $\alpha = 0°$.
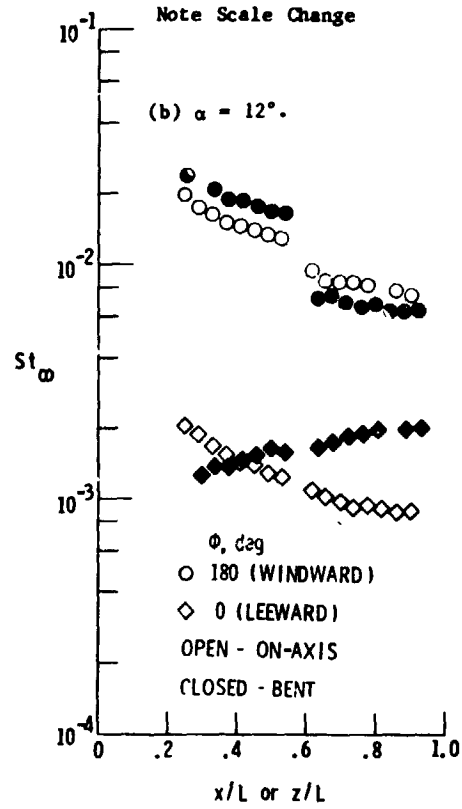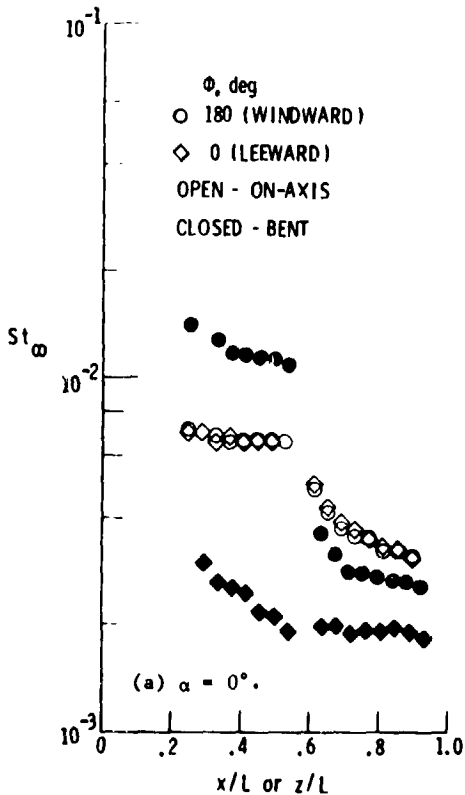
Fig. 6 Effect of nose bend on heating in air.

(c) $\alpha = 20°$.
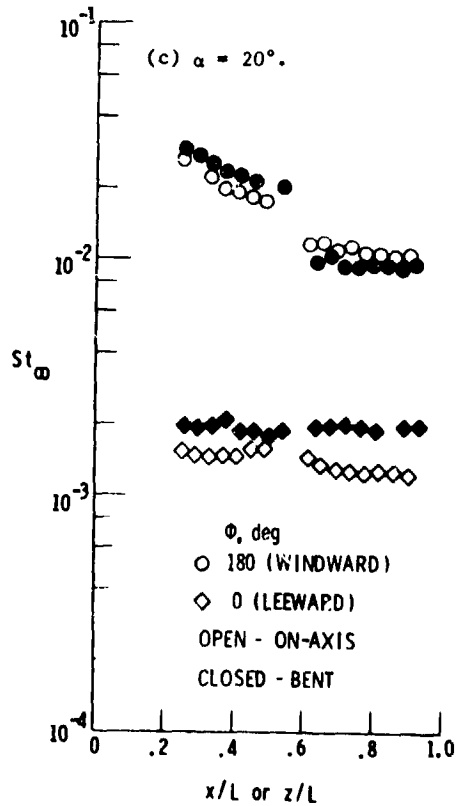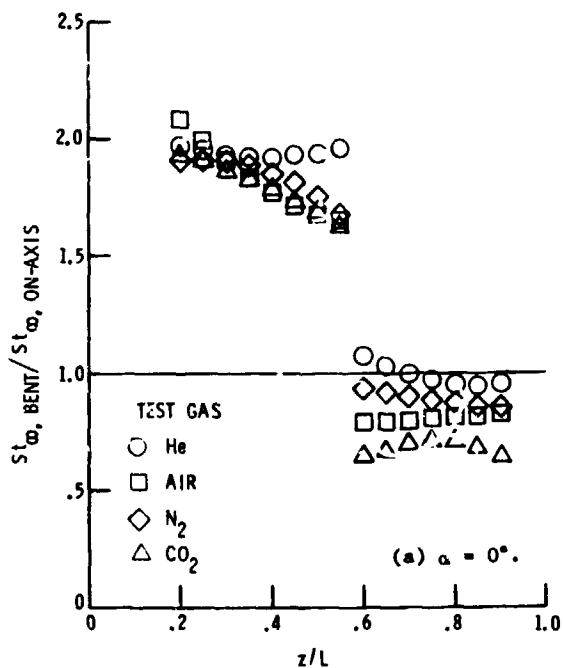
Fig. 6 Concluded.

Fig. 7 Ratio of bent biconic to on-axis biconic heating for present test gases.
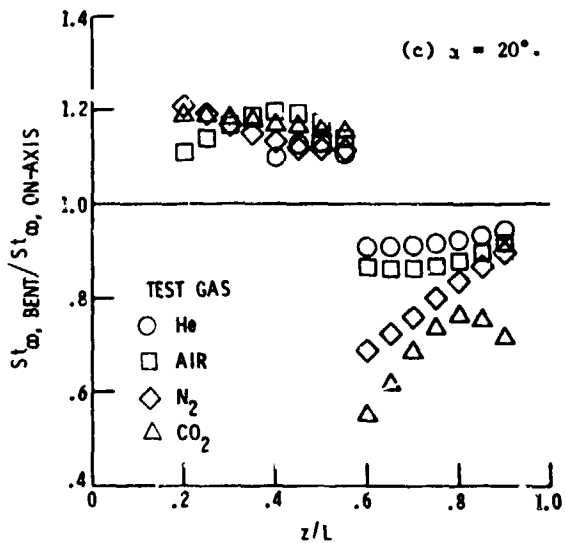
Fig. 7 Concluded.
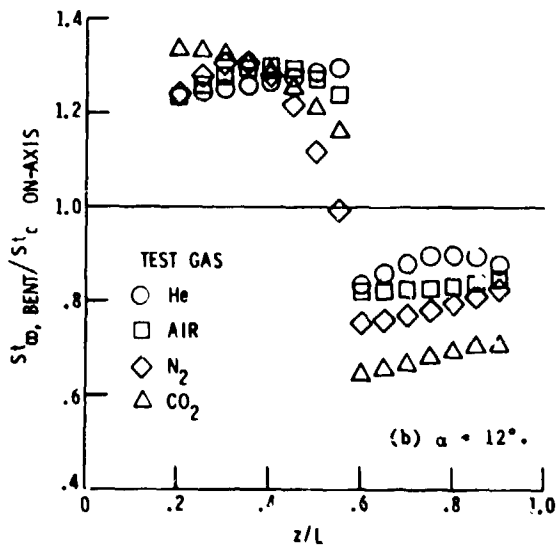
Fig. 7 Continued.
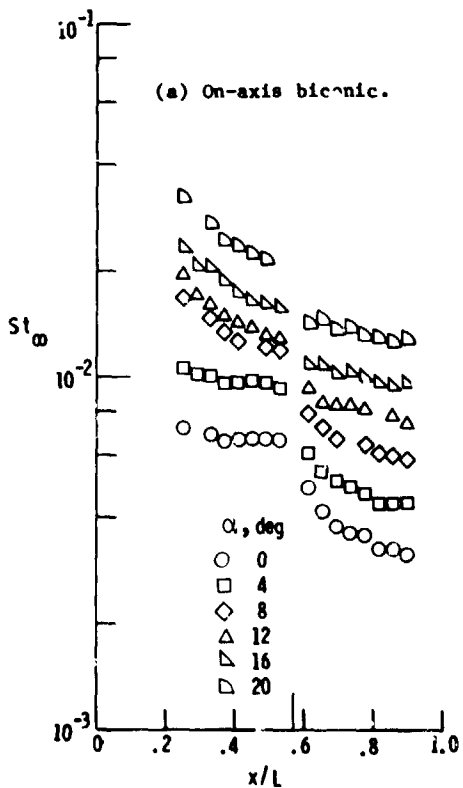
Fig. 8 Effect of angle of attack on windward heating in air.

(b) Bent biconic.

Fig. 8 Concluded.

(b) Bent biconic.

α, deg
- ○ 0
- □ 4
- ◇ 8
- △ 12
- ◁ 16
- ▷ 20

Fig. 9 Concluded.

α, deg
- ○ 0
- □ 4
- ◇ 8
- △ 12
- ◁ 16
- ▷ 20

(a) On-axis biconic.
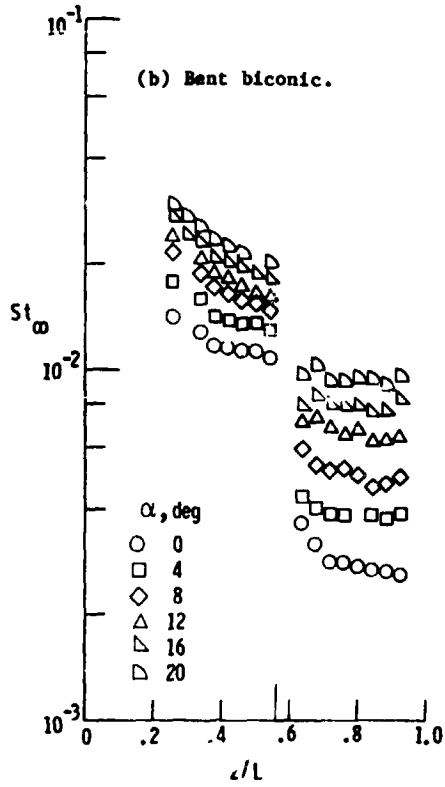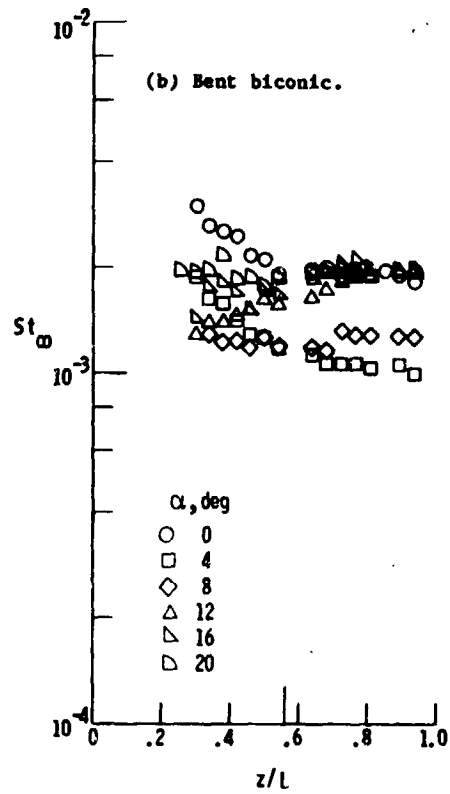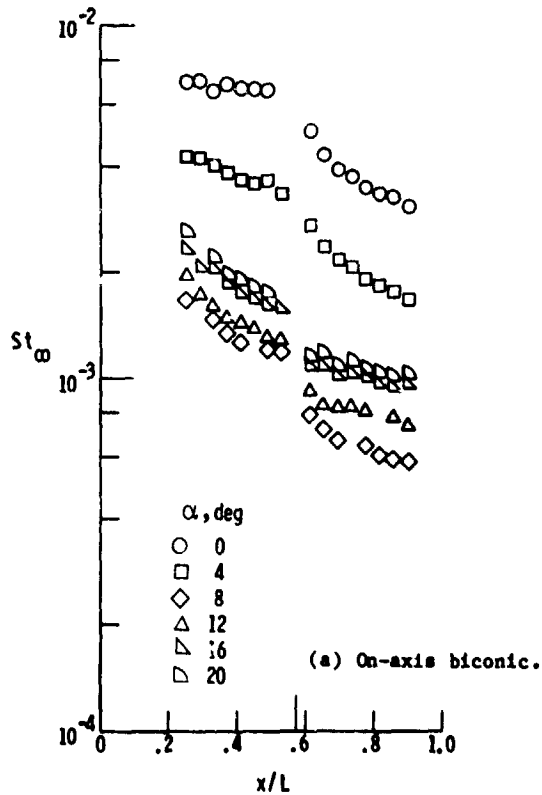
Fig. 9 Effect of angle of attack on leeward
heating in air.

TEST GAS
- ○ He
- □ AIR
- ◇ N_2
- △ CO_2

(a) $\alpha = 12°$.
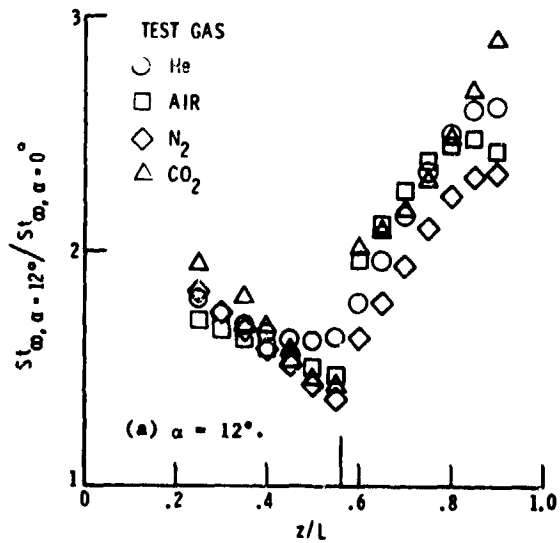
Fig. 10 Effect of angle of attack on windward
heating to bent biconic for present test
gases.

13

TEST GAS
○ He
□ Air
◇ N$_2$
△ CO$_2$

$St_{\infty, \alpha=20°}/St_{\infty, \alpha=0°}$

(b) $\alpha = 20°$.

z/L

Fig. 10 Concluded.

TEST GAS
○ He
□ Air
◇ N$_2$
△ CO$_2$

y/L

FLOW →

z/L

Fig. 12 Shock shapes for bent biconic at $\alpha = 4°$ in present test gases.

St_{∞}

x/L
○ .65
□ .90

θ, deg
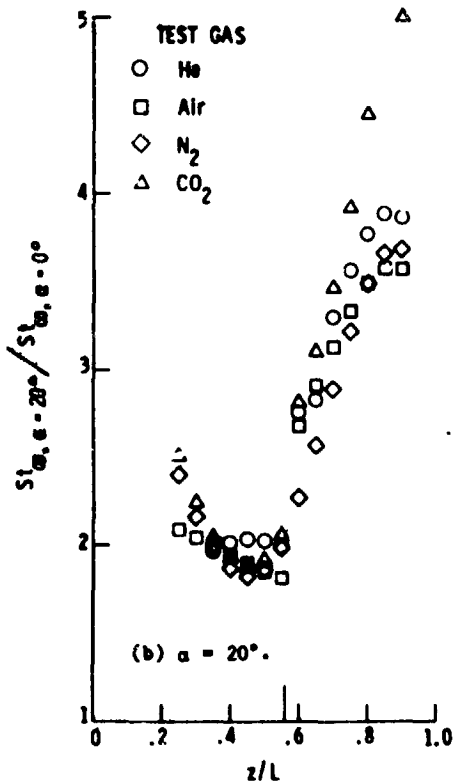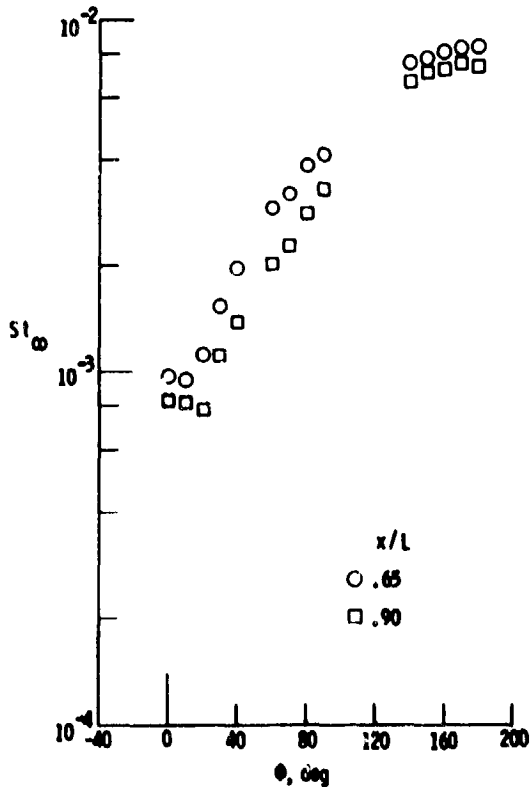
Fig. 11 Circumferential heating distribution for on-axis biconic in air at $\alpha = 12°$.

TEST GAS
○ He
□ Air
◇ N$_2$
△ CO$_2$

$\dot{q}/\dot{q}_{sph}$

(a) $\alpha = 0°$.

x/L
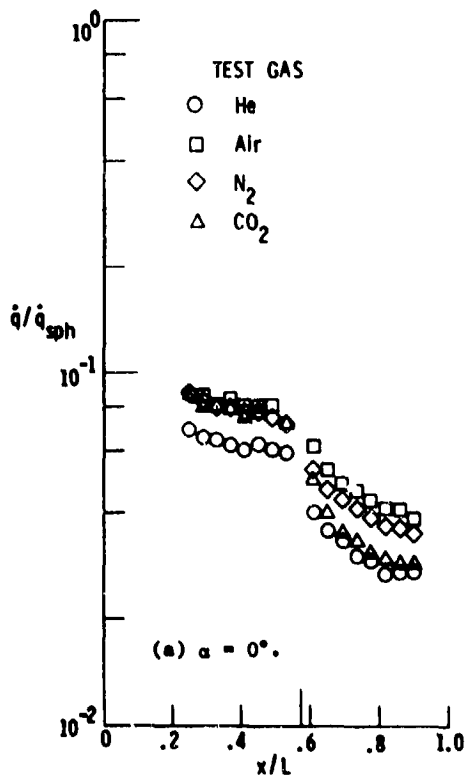
Fig. 13 Heating distributions for on-axis biconic in present test gases.

14
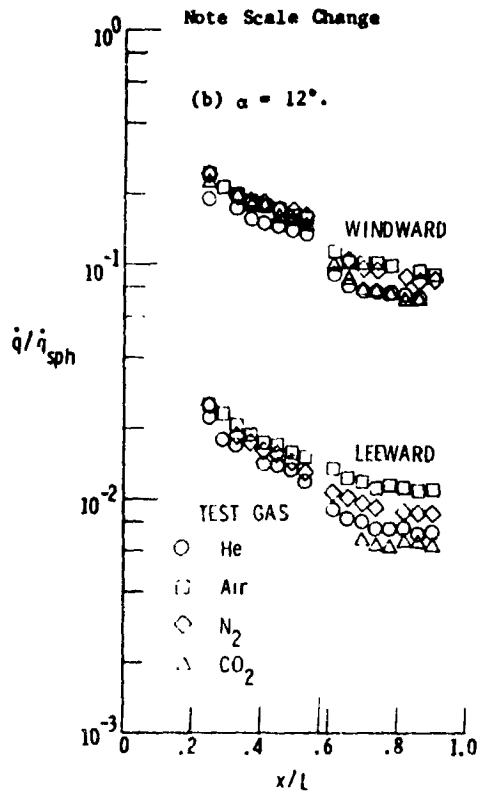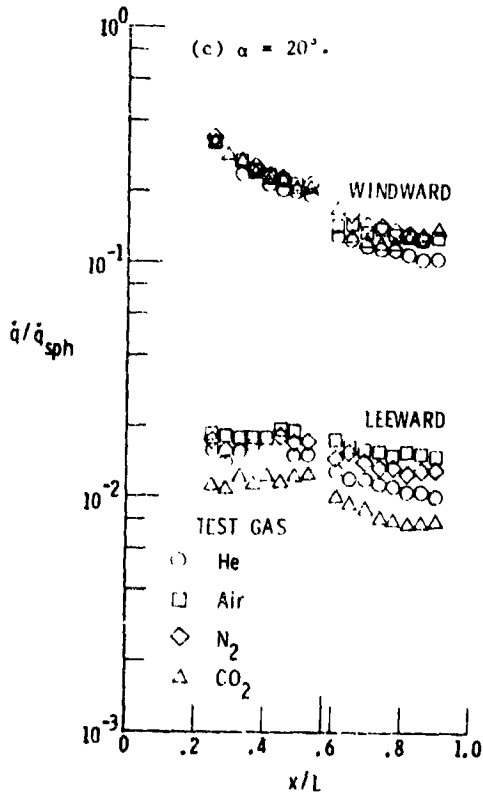
Fig. 13 Continued.

Fig. 13 Concluded.
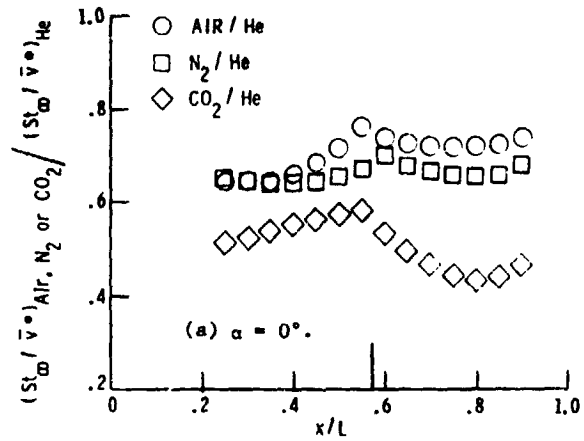
Fig. 14 Windward heating distributions in terms of a viscous-interaction parameter for on-axis biconic.
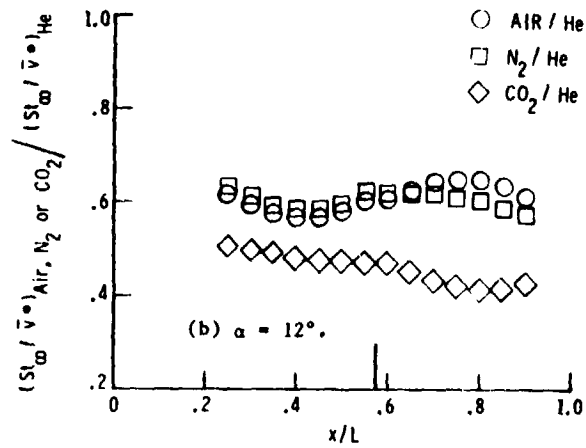
Fig. 14 Continued.
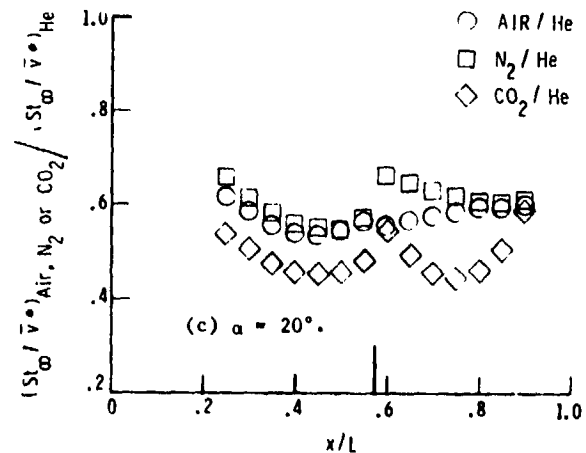
Fig. 14 Concluded.
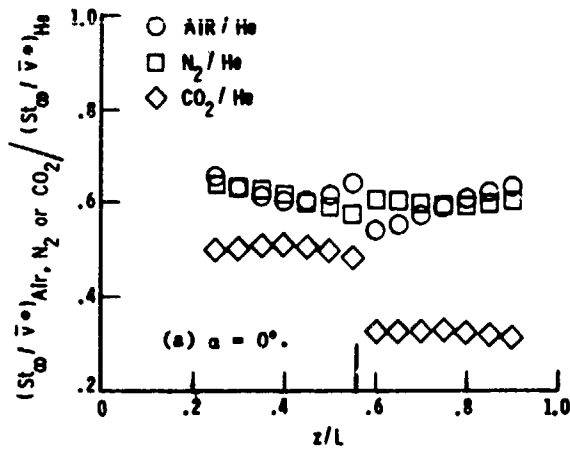
Fig. 15 Windward heating distributions in terms
of a viscous-interaction parameter for
bent biconic.
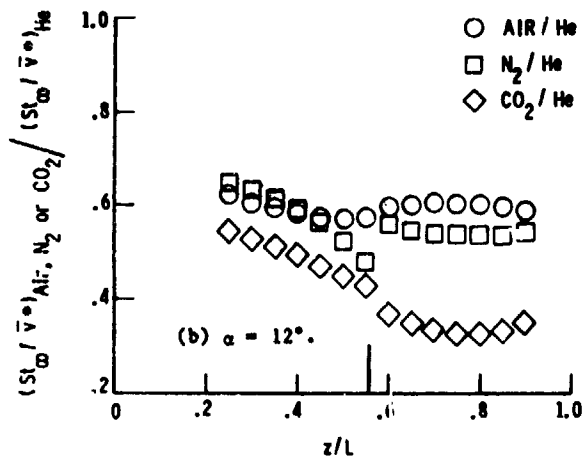
Fig. 15 Continued.
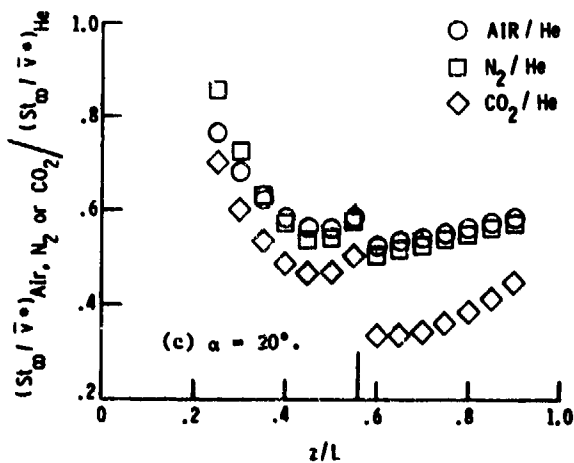
Fig. 15 Concluded.
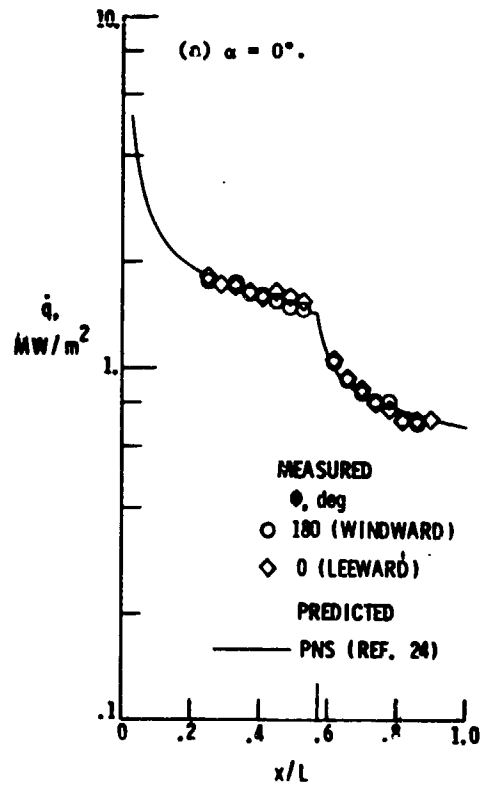
Fig. 16 Comparison of prediction to measurement
for on-axis biconic in helium.
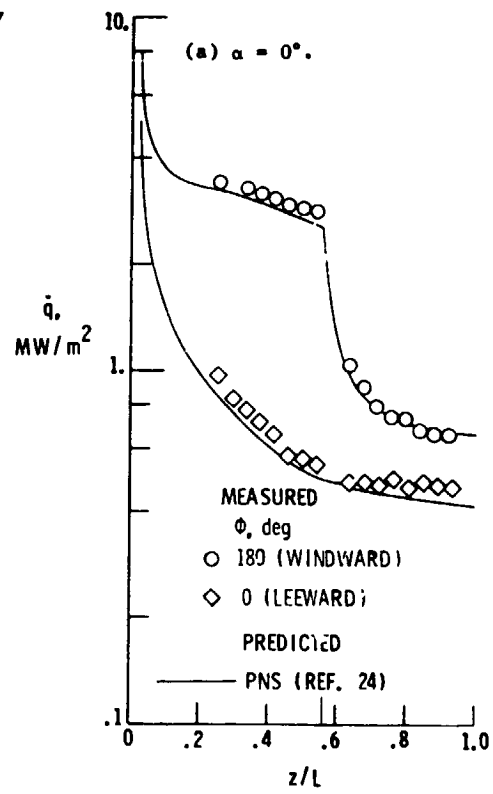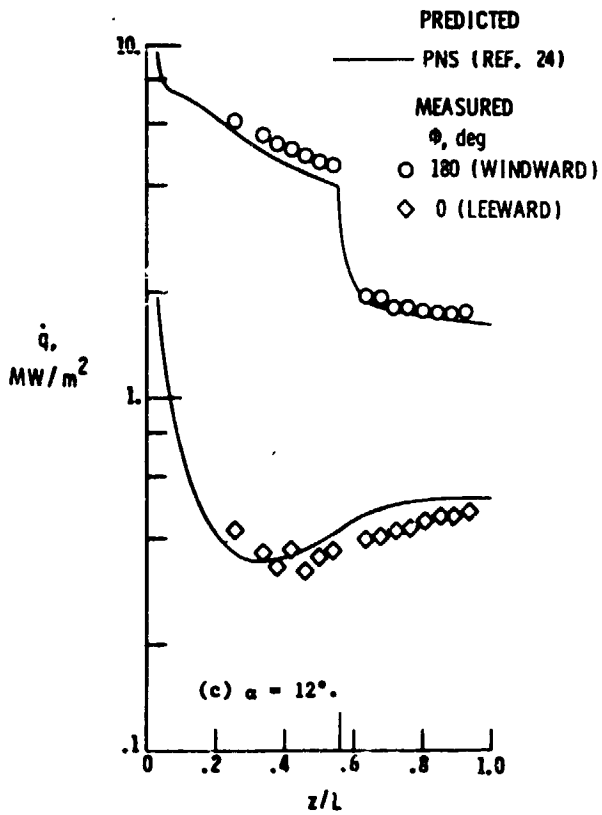
Fig. 16 Continued.

16
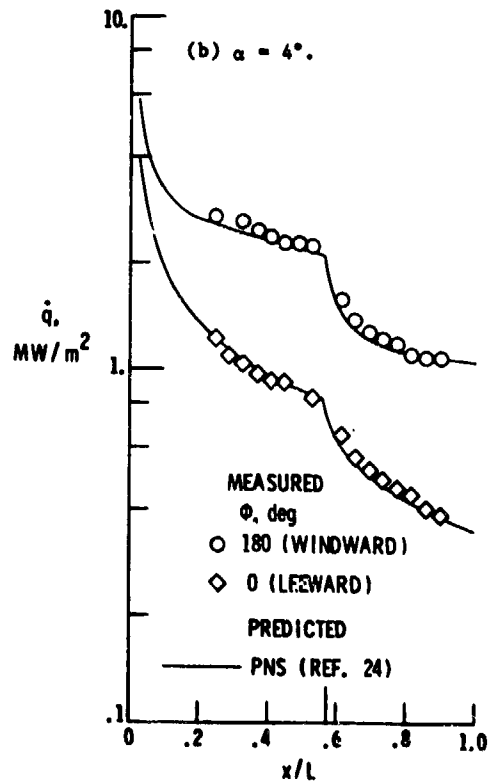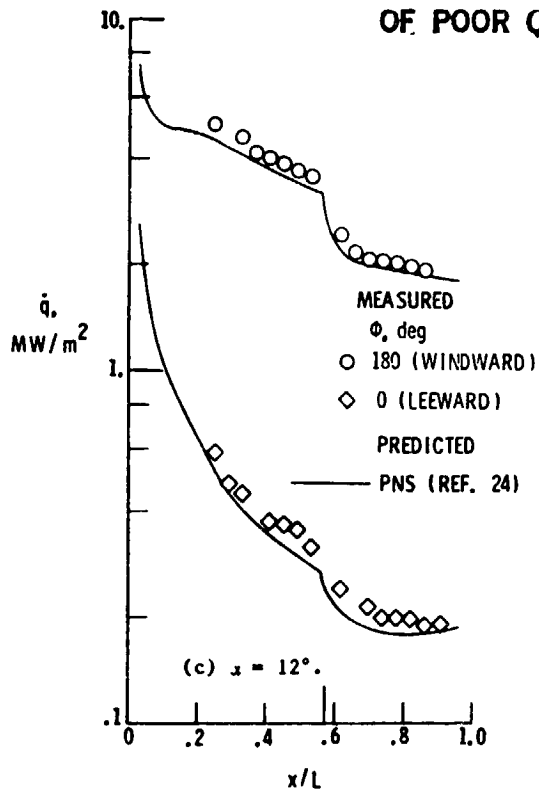
Fig. 16 Continued.

Fig. 17 Comparison of prediction to measurement
for bent biconic in helium.
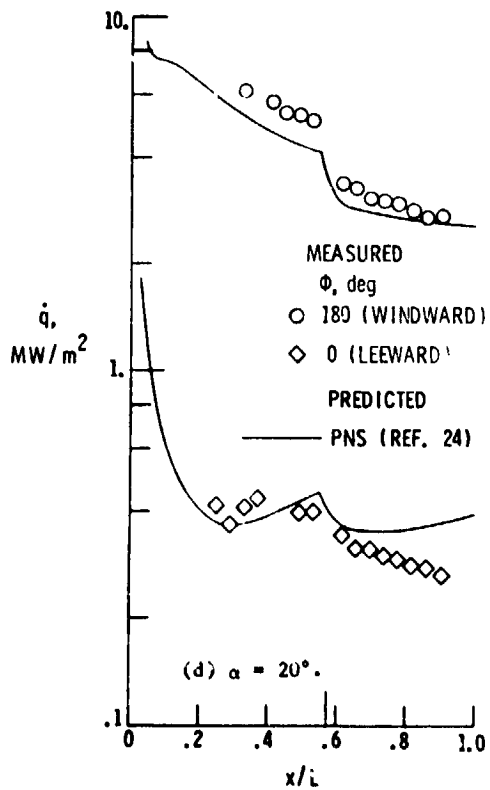
Fig. 16 Concluded.
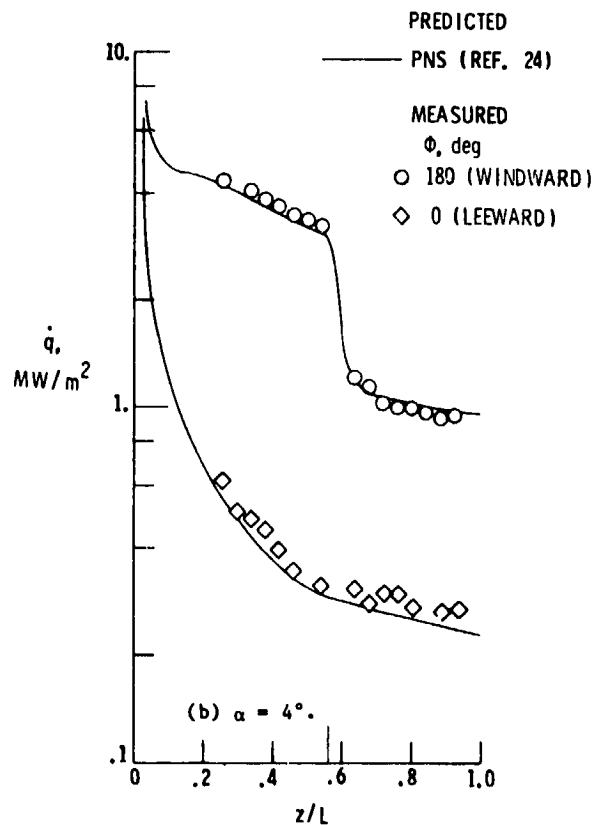
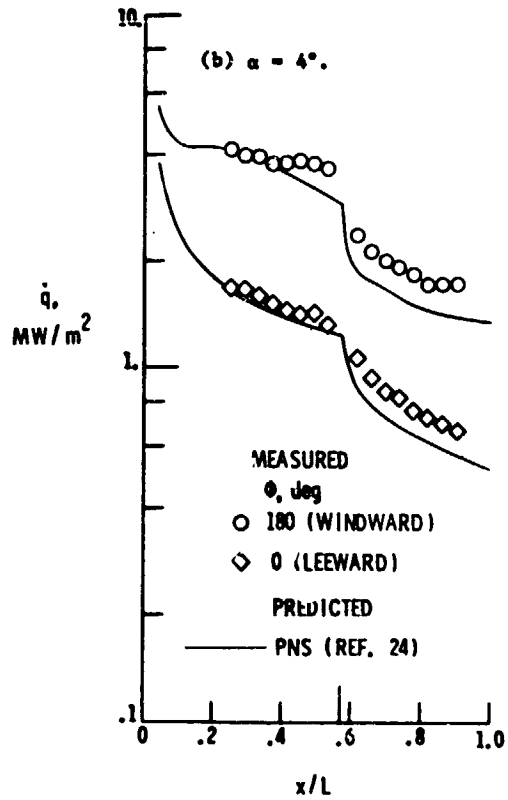Fig. 17 Continued.
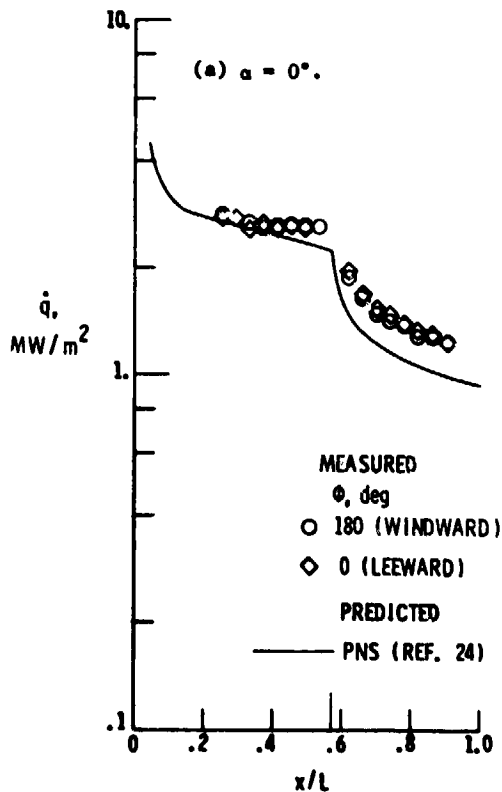
Fig. 17 Concluded.

Fig. 18 Concluded.

Fig. 18 Comparison of prediction to measurement
for on-axis biconic in air.